Reversible Electrochemical Gelation of Metal Chalcogenide Quantum Dots

Chathuranga C. Hewa-Rahinduwage,[†,‡] Xin Geng,[†,‡] Karunamuni L. Silva,[†,‡] Xiangfu Niu,[§] Liang Zhang,[§,||,*] Stephanie L. Brock,[†,*] and Long Luo[†,*]

[†] Department of Chemistry, Wayne State University, Detroit, Michigan 48202, United States

[§] School of Vehicle and Mobility, Tsinghua University, Beijing 100084, China

[||] Center for Combustion Energy, Tsinghua University, Beijing 100084, China

ABSTRACT: The ability to dictate the assembly of quantum dots (QDs) is critical for their integration into solid-state electronic and optoelectronic devices. However, assembly methods that enable efficient electronic communication between QDs, facilitate access to the reactive surface, and retain the native quantum confinement characteristics of the QD, are lacking. Here we introduce a universal and facile electrochemical gelation method for assembling metal chalcogenide QDs (as demonstrated for CdS, ZnS, and CdSe) into macroscale 3-D connected pore-matter nanoarchitectures that remain quantum confined and in which each QD is accessible to the ambient. Because of the redox-active nature of the bonding between QD building blocks in the gel network, the electrogelation process is reversible. We further demonstrate the application of this electrogelation method for a one-step fabrication of CdS gel gas sensors, producing devices with exceptional performance for NO_2 gas sensing at room temperature, thereby enabling the development of low-cost, sensitive, and reliable devices for air quality monitoring.

INTRODUCTION

Quantum dots (QDs) are prized for their unique and functional properties, associated with both intrinsic (quantum confinement) and extrinsic (high surface area) effects, as dictated by their size, shape, and surface characteristics.[1,2] As such, they have considerable promise for diverse applications, including energy conversion (thermoelectrics, photovoltaics), catalysis, and sensing.[1,3-7] In the past decade, much effort has been made to develop QD assembly methods that enable efficient electronic communication between QDs and retain the native quantum confinement characteristics, thus enabling fabrication of QD-based solid-state electronic and optoelectronic devices.[8-14] However, these methods are typically not suitable for fabrication of assemblies over large areas or in 3-D accessible formats; moreover, they are sensitive to defects and considerable room remains for improving their electrical transport properties. For applications in electrochemically-based sensors or catalysts, the ability to maximize available surface area is as important as the charge transport properties in dictating high activities.

QDs are typically prepared using solution-phase methods because these enable exquisite control over size, shape, and composition, in large part aided by the presence of ligands that passivate the surface of the particles as they form from monomer precursors.[15] However, the common long-chain organic moieties exploited for surface ligation necessarily restricts interparticle interactions as well as communication with the ambient.[16] While electron mobility can be enhanced by the exchange of the native ligands with short-chain organics (ethanedithiol, aniline) or inorganic ions (halides, chalcogenidometallates) either before or after film deposition (typically by dip- or spin-coating), the relatively high electronic resistivity remains a limiting factor in device performance.[7] Moreover, such "hybrid composites" have heterogeneous interfaces that moderate inter-particle communication, and the techniques involved for deposition lead to 2-D dense films that restrict interactions of the environment with the huge surface area intrinsic to QDs.

Here we demonstrate a new approach to QD assembly, electrochemical gelation or electrogelation, that produces macroscale 3-D connected pore-matter nanoarchitectures that remain quantum confined and in which each QD is accessible to the ambient. As shown in **Figure 1a** for the case of CdS, this is achieved by electrochemical removal (oxidation) of surface-bound thiolate ligand "protecting groups" as dithiolates and solvation of Cd ions, followed by oxidation of exposed "core" chalcogenides to form interparticle dichalcogenide bonds (e.g., $2S^{2-} - 2e \rightarrow S_2^{2-}$ for CdS QDs in **Figure 1a**). The redox-active nature of interparticle dichalcogenide bonds enables electrochemical disassembly of the gel network by reducing the dichalcogenide bonds to chalcogenides at negative potentials (**Figure 1a**). Importantly, the method is metal and chalcogen agnostic, as revealed by successful translation to ZnS and CdSe QDs. We further demonstrate that such gel structures can act as highly sensitive transducers, enabling detection of NO_2 with an unprecedented combination of a low limit of detection and rapid speed. The activity originates from the unique surface structure (as probed by DFT calculations), charge transport network, and the integrated pore-matter architecture of the QD gel. The approach is amenable to compositional and surface tuning enabling optimization for device applications from sensing to catalysis.

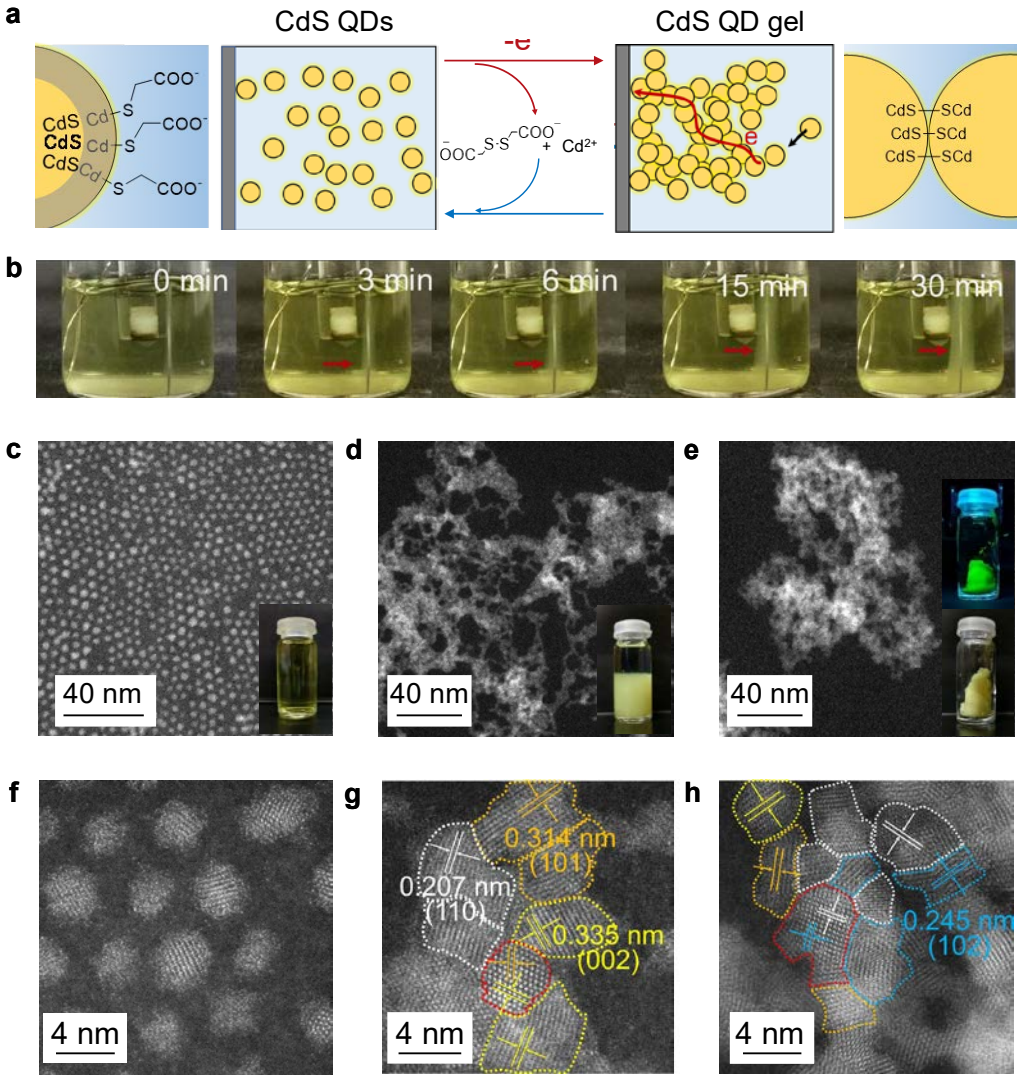

Figure 1. Electrogelation of CdS QDs. a, Schematic of reversible electrogelation of CdS QDs. QDs in solution first migrate to the anode where oxidation results in elimination of surface-bound thioglycolate (as dithioglycolate) and solvation of surface Cd ions to reveal core sulfide. Core sulfide is then oxidized to form disulfide bonds between QDs, yielding a gel network. Upon electrode potential reversal, the disulfide bonds are reduced to sulfides, disassembling the gel network. b, CdS gel growth on a Pt wire electrode as a function of electrogelation time at an electrode potential of 1.2 V vs. Ag/AgCl/sat. KCl reference electrode. c-e, Low-magnification STEM and TEM images of CdS QDs, wet gel, and aerogel, respectively. The insets show their corresponding photographs. Insets in e show a free-standing CdS aerogel under the ultraviolet (top) and normal light (bottom). f-h. High-resolution STEM images of CdS QDs, wet gel, and aerogel, respectively. Crystallites in the gel are color-coded according to their lattice fringes, corresponding to the (110), (101), (002), and (102) planes of hexagonal CdS. Crystallites in which two sets of planes are evident are outlined in red.

RESULTS AND DISCUSSION

Electrogelation of CdS QDs. Our inspiration for the electrogelation method is rooted in prior work from the Brock lab demonstrating chemical oxidation as a pathway to form monolithic gels and thin films of assembled metal-chalcogenide QDs linked by dichalcogenide bonds between particles.[17-21] Because a key attribute for exploiting quantum dot assemblies in microelectronic devices, solar cells, and electrochemical sensors is the need to marry the QDs to an electrode surface, we investigated electrooxidation as a method to gel QDs onto an active electrode directly. As proof of principle, we report the formation of CdS QD monolithic gels (electrogels) from Pt electrodes and compare the attributes of the wet gel and aerogel to chemically prepared gels (chemgels). We then demonstrate electrogelation of CdS on sensor supports to produce xerogel films for selective room-temperature sensing of NO_2 with low limit-of-detection (11 ppb), fast response-recovery times (<0.5 min), minimal variation in response during 400 NO_2 exposure/removal cycles (~7%), and exceptional reproducibility (<5% variation device-to-device).

For the electrogel formation, we first synthesized nearly-monodisperse sols of CdS QDs with an average diameter of 3.2 ± 0.4 nm (**Figure 1c**, **f**, and **Figure S1**) using a modified hot-injection method.[22] To facilitate the electron transfer between the QDs and electrode during electrogelation, we next performed a ligand exchange with a short-chain thiolate, thioglycolate. Electrogelation of CdS QDs was initiated by applying a potential of 1.2 V vs. Ag/AgCl/sat. KCl at a Pt wire anode immersed in the CdS QD solution. A layer of a pale-yellow translucent wet gel immediately started growing around the wire electrode upon applying the

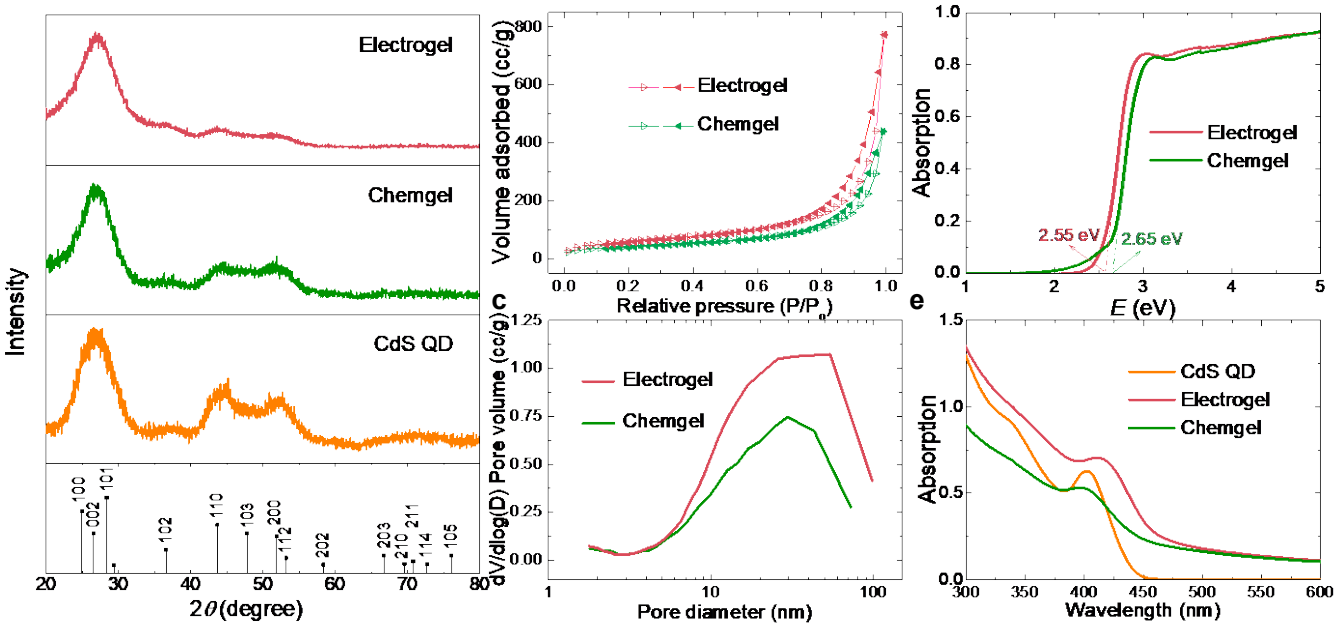

Figure 2. Characterization of electrochemically synthesized CdS aerogel (electrogel), chemically synthesized CdS aerogel (chemgel), and CdS QDs. a, Powder X-ray diffraction (PXRD) patterns. The stick diagram shows the PXRD pattern of hexagonal CdS (wurtzite) as a reference. b, nitrogen adsorption-desorption isotherms. c, Barrett-Joyner-Halenda pore size distribution plots. d, solid-state diffuse reflectance data (converted to absorption). e, solution-phase UV-visible absorption spectra.

potential (**Figure 1b**). Supercritical CO_2 drying yielded CdS aerogel monoliths with minimal volume loss compared to the wet gel. **Figure 1c-e** inserts show the photographs of a representative as-synthesized CdS QD solution, CdS wet gel, and CdS aerogel monolith; the CdS aerogel monolith is highly emissive even when excited with a handheld UV lamp. Electrogelation of CdS QDs capped with long-chain thiolates commonly employed in chemical gelation, such as 11-mercaptoundecanoate, was not effective under similar conditions (**Figure S2**), suggesting electrogelation of QDs relies on efficient electron transfer between QDs and electrode, which is inhibited with a long-chain thiolate capping agent.

Structural and Electronic Property Characterizations. Transmission electron micrographs of a CdS wet gel and aerogel (**Figure 1d, e**) produced by electrogelation show the presence of a mesoporous network (pore size from 2 to 50 nm). CdS QD building blocks are visible in the gel network (**Figure 1g, h**), having ripened modestly during the electrogelation, resulting in a broader size distribution shifted to larger average sizes (~ 4 nm) relative to the native quantum dots (3.2± 0.4 nm). These building blocks are crystalline and randomly oriented, as evidenced by the presence of different lattice fringes corresponding to the (110), (101), (002), (102) planes of hexagonal CdS. We further characterized the crystallinity of electrochemically prepared CdS aerogel (electrogel) using powder X-ray diffraction (PXRD). The electrogel exhibited the characteristic peaks of hexagonal CdS (PDF 00-001-0780, **Figure 2a**). The peak widths at half height were similar for the electrogel and CdS QDs suggesting the average crystallite size is not significantly changing in the process, which is consistent with the electron microscopy results. The porosity of the electrogel was analyzed by nitrogen physisorption, which produced a type-IV isotherm, characteristic of a mesoporous material (**Figure 2b**). The surface area of the electrogel was 220 m^2/g based on the Brunauer–Emmett–Teller model.[23] **Figure 2c** illustrates the pore-size distribution for electrogel, which was obtained by fitting the Barrett–Joyner–Halenda model using the desorption branch of the isotherm.[24] The average pore diameters and cumulative pore volumes were calculated to be 20.5 nm and 1.2 cm^3/g, respectively. For comparison, a CdS aerogel sample was also synthesized using the traditional chemical gelation method (chemgel). The chemgel shows a similar PXRD pattern as the electrogel, but its surface area (155 m^2/g), average pore diameter (17.2 nm), and cumulative pore volume (0.68 cm^3/g) are slightly lower than that of the corresponding electrogel (**Table S1**).

The bandgap values of the electrogel and chemgel were measured by diffuse reflectance spectroscopy (**Figure 2d**). The absorption onsets for electrogel and chemgel are 2.55 eV and 2.65 eV, respectively, both of which are greater than that for a bulk CdS solid (2.42 eV).[25] This suggests that the nanoparticle chromophores remain quantum confined, despite the fact that they are linked together in a 3-D network. This is attributed to the fractal connectivity of the network and/or the characteristics of grain boundaries at the interfaces. On the other hand, the slightly smaller bandgap for electrogel relative to chemgel may be a consequence of resonance transfer between particles of slightly different sizes and/or gradients in the fractal dimensionality that arise from the voltage drop as the gel grows farther from the electrode surface. A small redshift of ~10 nm in the UV-Vis spectra for the electrogel relative to the chemgel and CdS QDs (**Figure 2e**) is consistent with the bandgap results. Additionally, note that the green emission

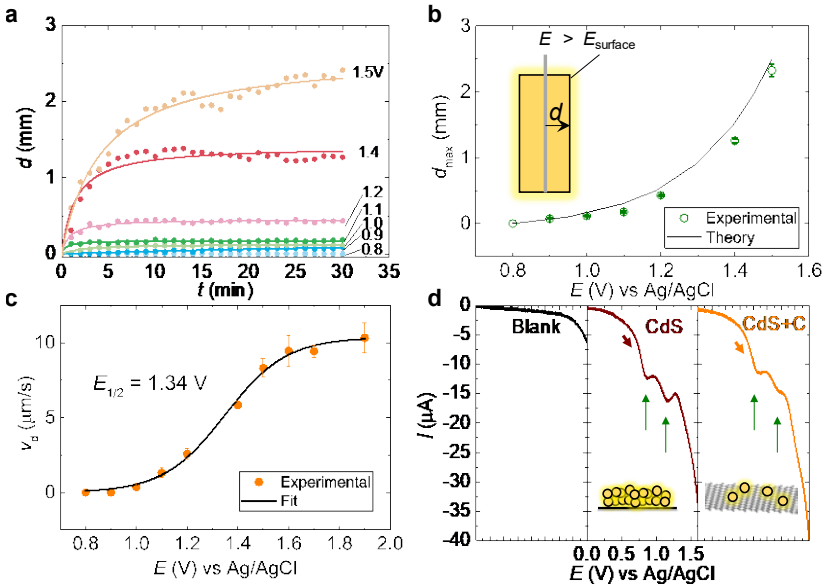

Figure 3. Kinetics and thermodynamics of CdS electrogelation. a, Electrogel thickness (d) vs electrogelation time (t) at different electrode potentials (E). b, Maximum electrogel thickness (d_{max}) vs. electrode potential (E). d_{max} is the average electrogel thickness between t = 20 and 30 min. Error bars are the corresponding standard deviations. c, Initial growth rate (v_d) as a function of E. v_d was estimated from the electrogel thickness in the first 400 s of electrogelation time. Error bars are the standard deviations of the slopes from the linear fitting. d, Linear sweep voltammograms of CdS QDs and CdS QDs supported on carbon (CdS+C). The samples were prepared by drop-casting CdS QDs or CdS+C onto a glassy carbon electrode and then dried in a flow of N_2 gas before the measurements. The blank used an unmodified glassy carbon electrode.

(**Figure 1e**, inset) is consistent with previous observations of trap state emission from CdS chemgels.[19] Overall, our electrogelation method produces CdS gels that are structurally and electronically like the chemgel, but with a drastically shortened gelation time (~30 min for electrogelation vs. several hours to several days for chemical gelation).[17-21, 26]

Electrogelation Mechanism. To unravel the electrogelation mechanism, we studied the kinetics of electrogelation by measuring the gel thickness (d) as a function of electrogelation time (t) at various electrode potentials (E). CdS gel formation was noticeable when E > 0.8 V (**Figure S3**). At a fixed E, d increases with t until it reaches a plateau value, d_{max} (**Figure 3a**), indicating electrogelation is a self-limiting process. The d_{max} arises because the semiconductive CdS gel lowers the potential on the gel surface ($E_{surface}$< E) as the gel grows, and, eventually, stops the gel growth when the gel becomes sufficiently thick. The d_{max} increases non-linearly with E (**Figure 3b**). The experimental plot of d_{max} vs. E is in excellent agreement with the theoretical prediction from a simple model that assumes there is a significant iR drop in the gel (see the model details in **Figure S4**), which validates the explanation. The self-limited gel growth gives significant technological prospects due to easier control over film thickness.

The initial gel growth rate (v_d) was also extracted from the gel growth curve in the first 400 s. The dependence of v_d on E shows a sigmoidal curve (**Figure 3c**), which is the characteristic feature for an electrochemical reaction transitioning from a reaction kinetics-limited process to a diffusion-limited process, *i.e.*, from reaction-limited cluster aggregation to diffusion-limited cluster aggregation.[27] These kinetic processes also occur upon chemical oxidation, and are responsible for the formation of the solvent-supported gel network in lieu of a bulk precipitate (kinetic barrier too low) or a stable colloid (kinetic barrier too high).[28] The standard potential for electrogelation of CdS QDs can be estimated from the half-wave potential ($E_{1/2}$) to be ~1.34 V.

During CdS QDs electrogelation, there are two possible electrooxidation steps: (1) cleavage of the X-type Cd-S (thioglycolate) bond on the QD surface with concomitant formation (elimination) of dithioglycolate and (2) formation of S-S disulfide bonds between CdS QDs. The $E_{1/2}$ value measured from the electrogelation kinetics study should reflect the more challenging step between the two. To identify their corresponding oxidation potentials, we designed and performed the following experiments. First, we acquired the linear sweep voltammogram of thioglycolate-capped CdS QDs. Two distinct anodic peaks are present at ~0.8 V and 1.2 V (**Figure 3d**), consistent with the two proposed oxidation steps during gelation. Second, we prepared a CdS+C sample, where CdS QDs were immobilized on a carbon support. In CdS+C, CdS QDs are largely (although not exclusively) isolated from each other (**Figure S5**). The physical separation between QDs prevents the formation of S-S bonds between CdS QDs but does not interrupt the oxidative removal of thioglycolate (as dithioglycolate) from the CdS QD surface. The linear sweep voltammogram of CdS+C in **Figure 3d** shows a similar peak at 0.8 V as CdS QDs and a significantly diminished peak at 1.2 V. This finding suggests the anodic peak at 0.8 V should correspond to the thioglycolate ligand removal and the peak at 1.2 V arises from the S-S bond formation. The S-S bond formation is presumed to be rate-limiting for electrogelation based on the similarity of its corresponding potential (1.2 V) to the $E_{1/2}$ value obtained above (1.34 V).

The thioglycolate ligand removal during electrogelation was further confirmed by Fourier transform infrared

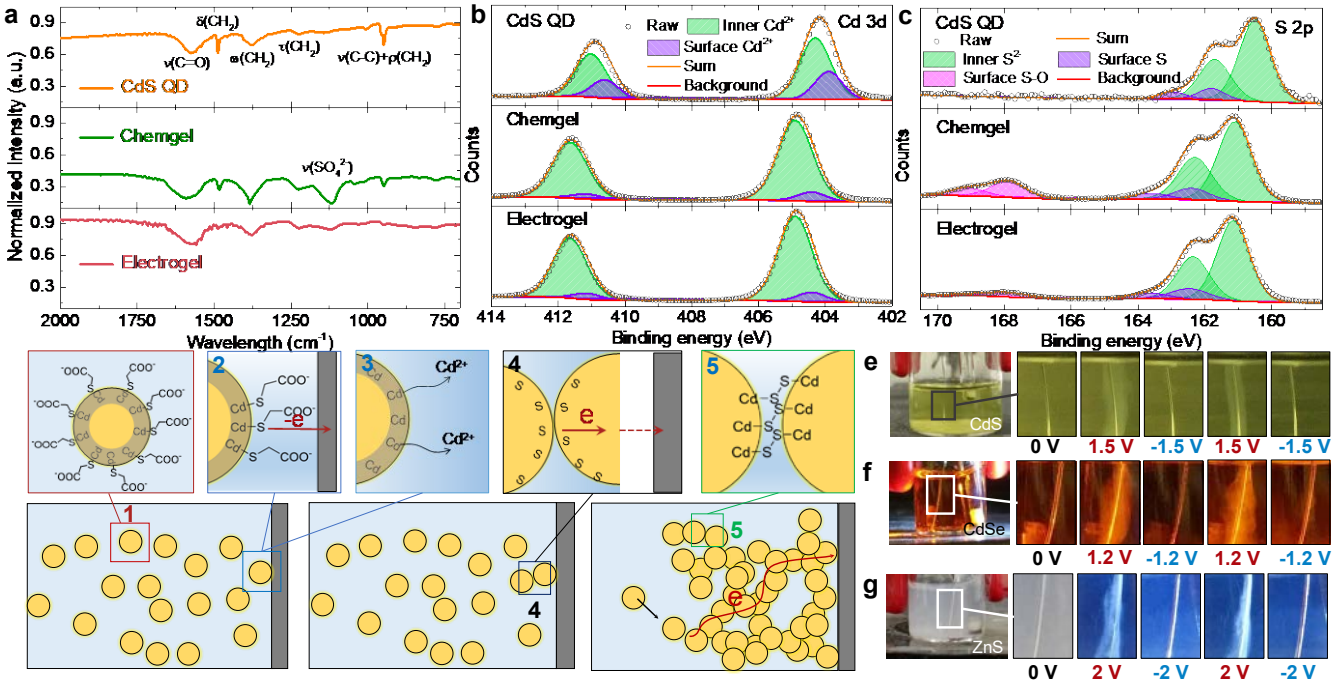

Figure 4. Mechanistic studies of QD electrogelation. a, Fourier transform infrared spectroscopy (FTIR) of CdS QDs, chemgel, and electrogel. b-c, X-ray photoelectron spectroscopy (XPS) showing the Cd 3d and S 2p regions of CdS QDs, chemgel, and electrogel. d, Schematic illustration of electrogelation of CdS QD. **1**, Thioglycolate-capped CdS QDs are suspended in methanol. **2**, When a QD collides at the anode, thioglycolate is removed by electrochemically cleaving the Cd-thioglycolate bond and eliminating dithioglycolate. **3**, Next, the exposed Cd ions on the QD surface detach (are solvated), exposing sulfide at the surface. **4** and **5**, The QDs are cross-linked by electrochemically oxidizing the surface sulfide to form disulfide bonds between particles. **4** and **5** are electrochemically reversible. e-g, Reversible electrogelation of CdS, CdSe, and ZnS QDs, respectively.

spectroscopy (FTIR). **Figure 4a** shows the FTIR spectra of CdS QDs, chemgel, and electrogel. The signals were normalized by the Cd content in these samples. In comparison to CdS QDs, the chemgel and electrogel show attenuated intensities for CH_2 in-plane scissoring band at 1486 cm^{-1}, the C-C stretching band and CH_2 in-plane bending band at 948 cm^{-1}, all of which are associated with thioglycolate ligands.[29] We also noticed a new band emerging at 1114 cm^{-1} corresponding to the asymmetric stretching band of sulfate for gel samples (in particular, for the chemgel), possibly due to the partial oxidation of surface S to sulfate during gelation.[30]

X-ray photoelectron spectroscopy (XPS) was also performed to investigate the surface property changes during electrogelation. **Figures 4b** and **4c** show the XPS spectra of CdS QDs, chemgel, and electrogel in the Cd 3d and S 2p regions. For all Cd 3d spectra, two pairs of peaks are apparent after fitting the spectra by a composite function (30% Lorentzian+70% Gaussian). The pair of peaks in purple at lower binding energies are assigned to the surface Cd atoms, and the other pair in green at higher binding energies to the interior Cd atoms.[31] For CdS QDs, the surface Cd peaks are located at 403.90 eV and 410.60 eV. In comparison, the surface Cd peaks for the two gel samples shift to higher binding energies at 404.40 eV and 411.15 eV due to the change in surface composition induced by the gelation process. Analysis of the peak areas reveals that the surface Cd percentage decreases significantly from 28% in CdS QDs to ~8% in the gel samples (**Table S2**).

Similarly, two pairs of peaks are present in the S 2p spectrum of CdS QDs, corresponding to the surface and interior S atoms.[31] These two pairs of peaks slightly shifted to high binding energies for gels as well, possibly because of the formation of S_2^{2-} species during gelation.[18] Another distinct feature of the S 2p spectra for gels is that a pair of new peaks (highlighted in pink, **Figure 4c**) appears at 167.88 eV and 169.08 eV, indicating the formation of S-O species.[32] This observation is consistent with the emergence of an asymmetric stretching band of sulfate in the FTIR spectra of the gel samples. Assuming the S-O species are on the gel surface, we estimated the total percentage of surface S (including the surface S and S-O species) from the peak areas to be ~25 % in the gel samples, a 2.5-fold increase relative to the CdS QDs (**Table S2**). The above XPS results show the surface percentages of Cd and S have almost completely flipped for CdS QDs and gels (**Figure S6**).

Taken together, we propose the following electrogelation mechanism, as illustrated in **Figure 4d**. Thioglycolate-capped CdS QDs are originally suspended in methanol. When a QD collides at the anode, thioglycolate is first removed by electrochemically cleaving the Cd-S (thioglycolate) bond (the oxidation potential is ~0.8 V) and eliminating dithioglycolate. Next, the exposed Cd ion on the QD surface detaches due to solvation in methanol, possibly aided by the presence of carboxylate in the departing

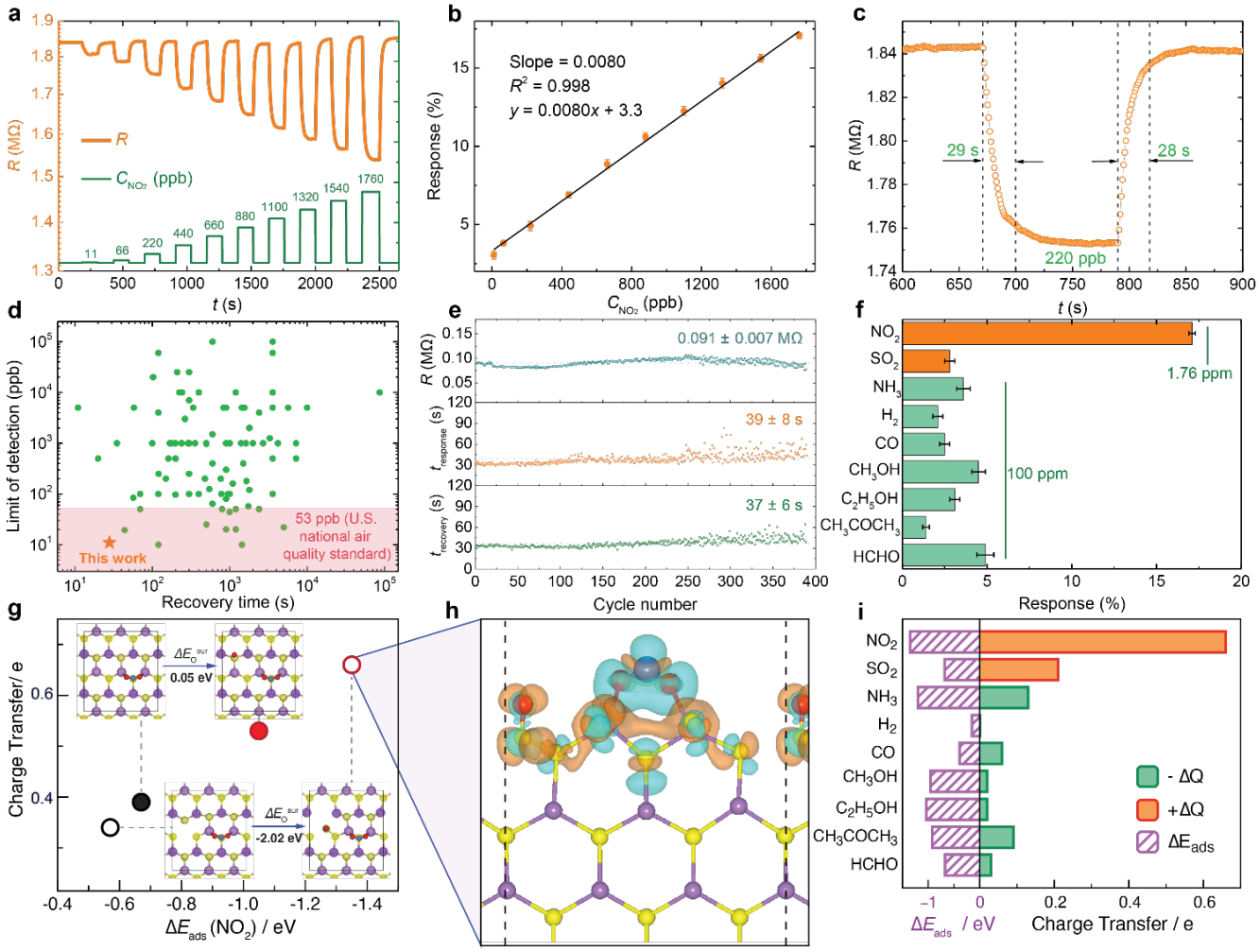

Figure 5. Gas sensing performances of CdS gel sensors at room temperature. a, Response-recovery curve of a CdS gel sensor to NO_2 at different concentrations (11-1760 ppb). b, Sensor response (S) vs. NO_2 concentration (C_{NO_2}). c, Response-recovery curve in the presence of 220 ppb of NO_2. d, Comparison to 100 state-of-the-art room-temperature NO_2 gas sensors in literature. e, Stability performance of a CdS gel sensor during 400 response–recovery cycles. f, Responses of a CdS gel sensor to different 100 ppm gases at room temperature (NO_2 and SO_2 concentrations are 1.76 ppm). g, DFT calculated NO_2 adsorption energy ($\Delta E_{ads}(NO_2)$) and the corresponding charge transfer on a pristine CdS (100) surface (CdS, black filled circle), with one surface Cd vacancy ($CdS_{V_{Cd}}$, black open circle), with one surface S oxidized (CdS_{SO_x}, red filled circle), and with one Cd vacancy and one residual S oxidized ($CdS_{V_{Cd}+SO_x}$, red open circle), respectively. Insets are top views of corresponding surface structures. Cd, S, N, and O atoms are shown as purple, yellow, blue, and red balls, respectively. Calculated surface S oxidation energy (ΔE^{O}_{surf}) of −2.02 eV indicates that the presence of a Cd vacancy facilitates the surface S oxidation. h, Calculated differential valence-electron charge densities of NO_2 adsorption on $CdS_{V_{Cd}+SO_x}$ ($\Delta\rho = \rho_{NO_2^*} - \rho_* - \rho_{NO_2}$); charge depletion and accumulation are illustrated by orange and cyan regions, respectively (isosurfaces are set to 0.001 e/Å²). i, Calculated adsorption energies (left) and charge transfer values (right) for different gases on $CdS_{V_{Cd}+SO_x}$. The charge transferred from and to the CdS surface is plotted in orange and green, respectively.

dithioglycolate, producing an S-rich surface, as evidenced by the high percentage of surface S in the gels. The QDs are then cross-linked by electrochemically oxidizing the surface sulfide to form S-S disulfide bonds (the oxidation potential is ~1.2 V). The presence of disulfide linkages was confirmed by the dissolution of an electrogel upon applying a negative potential to reduce $[S\text{-}S]^{2-}$ bonds back to $2S^{2-}$ (**Figure 4e**).[18] Because electrogelation relies on effective electrochemical reactions of QDs, when CdS QDs are capped by long-chain thiolates, or when the CdS gel grows to a certain thickness, the electrode reactions are hindered, leading to slow or no gelation.

This new electrogelation method was also found to be universally applicable to metal chalcogenides. **Figure 4f** and **g** show the reversible electrogelation of CdSe and ZnS QDs. Just as in CdS electrogelation, ZnS gelation is caused by the electrochemical formation of S-S bonds. In the case of CdSe QD gelation, Se-Se bonds form between QDs by oxidizing Se^{2-} on the QD surface, analogous to the sulfide case.[33]

NO_2 Gas Sensing Performance and Mechanism. Our electrogelation method provides a facile approach for fabricating a mesoporous semiconducting QD network in one step, making it well-suited for preparing QD-based electrochemical sensing devices. While the presence of disulfide linkages might appear to be disadvantageous for facile electron transfer between particles, potentially serving as an electron getter and resulting in reductive cleavage of the network, previous experiments on chemically produced CdSe xerogel films (micron thickness) revealed conductivities on the order of 10^{-3} S/cm (van der Paaw),[34] and related 70 nm thin films produced stable photocurrents of ~75 $\mu A/cm^2$ upon illumination with white light (100mW).[35] Moreover, previous work also demonstrated that 1 cm diameter monoliths of CdSe aerogels (chemically produced) exhibit ratiometric responses in photoluminescence emission intensity to triethylamine; the success of this endeavor was attributed in part to the large, accessible surface area.[36] Accordingly, we hypothesized that electrogels exhibiting facile conduction pathways and high surface areas should be ideal platforms for electrochemical sensor development.

For our initial foray into electrochemical sensing devices, we demonstrate the application of CdS electrogels for room-temperature NO_2 gas sensing. This analyte was selected because low-cost, sensitive, and reliable NO_2 sensors are lacking for air quality monitoring by citizens and community groups.[37] We prepared CdS gel sensors by direct electrogelation of CdS QDs on a sensor substrate patterned with interdigitated electrodes, followed by drying in air (**Figure S7**). The sensor performance was tested at room temperature using a home-built apparatus (**Figure S8**). The sensor response is defined as $S = |R_a\text{-}R_g|/R_a$, where R_a and R_g are the resistance of a sensor in the presence of air and target gas, respectively. Upon exposure to NO_2, the sensor resistance decreases, characteristic of a p-type semiconductor.[38] **Figure 5a** shows the response of a CdS gel sensor towards NO_2 at various concentrations from 11 ppb to 1.76 ppm. The resistance decreased rapidly when NO_2 was introduced and swiftly recovered once NO_2 was removed. There is excellent linearity between the sensor response and NO_2 concentration for ppb-level NO_2 (R^2 = 0.998, **Figure 5b**). The CdS gel sensor also shows fast response-recovery dynamics at room temperature; for example, the response and recovery times for 220 ppb NO_2 are 29 and 28 s, respectively (**Figure 5c**). **Figure 5d** summarizes the limit of detection (LOD) and the recovery time of the CdS gel sensor and 100 state-of-the-art room-temperature NO_2 gas sensors in the literature (see **Table S3**). As is evident from **Figure 5d**, previously reported sensors with rapid recovery times (< 30 s), suffer from high LODs (≥ 500 ppb),[39, 40] whereas those with low LODs (≤ 30 ppb) tend to have slower recovery times (≥ 44 s, typically 100's of s).[41-48] This is not surprising since low LODs are favored by high analyte binding energies that render the coordinated analyte difficult to displace. Notably, the CdS gel sensor has the best combination of low LOD (11 ppb) and rapid recovery time (28 s) at room temperature.

In addition to low LOD and rapid recovery time, cycling stability and analyte selectivity are essential for the design of practical sensors. As shown in **Figure 5e** and **Figure S9**, the variation in response for the CdS gel sensor over 400 NO_2 exposure/removal cycles, is, impressively, only ~7%. The response and recovery times are also consistent at 39 ± 8 s and 37± 6 s over the 400 cycles. Likewise, as shown in **Figure 5f**, the response of CdS gel sensors to NO_2 is at least 3.5 times higher than other common gases or vapors including sulfur dioxide (electron acceptor), ammonia, hydrogen, carbon monoxide, methanol, ethanol, acetone, and formaldehyde (electron donors), even when the concentrations of the electron-donating molecules are > 50-fold that of NO_2. Our one-step electrogelation method not only simplifies the sensor fabrication procedure—which will undoubtedly lower the production cost—but also dramatically improves the reproducibility among devices. Indeed, we tested 10 independently prepared gel sensors and found a remarkably low device-to-device variation of < 5% (**Figure S10** and **Table S4**).

The exceptional sensing performance of the CdS gels arises from their unique mesoporous QD network and surface chemistry. According to the classical theory of semiconductor gas sensing,[49] sensing performance, especially sensitivity, is controlled by three independent factors: (1) accessibility of the active (sensing) sites to the target gas, (2) the nature of the interaction between the active site and the gas-phase analyte; and (3) how the surface interactions are converted into the electrical signal (transduction).

The nature of the CdS gel structure—specifically, the interconnected pore-matter architecture—addresses Factor 1 by enabling efficient gas exchange throughout the gel network, facilitating interactions between the analyte and the QD surfaces, and thus, rapid response.[50] Factors 2 and 3 are more challenging to address experimentally, so we turned to computational methods. Specifically, we studied NO_2 adsorption on CdS surfaces using density functional theory (DFT) calculations with Van der Waals correction. As discussed previously, the thioglycolate ligands on the surface are removed during electrogelation, the exposed CdS gel surface is enriched with S and surface S is partially oxidized (**Figure 4**, **Figure S11**, and **Table S5**). We evaluated the effects of these surface features on NO_2 adsorption using four surface models of CdS (100): a pristine CdS surface, a CdS surface with a single Cd vacancy, a CdS sur-

face with a single oxidized S site, and a CdS surface with both a Cd vacancy and residual S oxidized (**Figure 5g** and **Figure S12**). Note that the presence of a Cd vacancy is used to simulate an S-enriched CdS surface. **Figure 5g** shows the adsorption of NO_2 is strongest on the CdS surface with both Cd vacancy and residual S oxidized (red open circle). Also, it shows adsorption of NO_2 is significantly strengthened in the presence of oxidized S sites (compare pristine CdS, black filled circle, with oxidized CdS surface, red filled circle). The unoxidized S-rich surface (Cd vacancy, black open circle), however, slightly weakens the NO_2 adsorption relative to the pristine surface. Intriguingly, the oxidation of S on the S-rich (Cd-vacancy) surface is an energetically more favorable process (the O binding energy on S, $\Delta E^{O}_{surf} = -2.02$ eV**, Figure 5g** insert), relative to oxidation of the pristine surface ($\Delta E^{O}_{surf} = 0.05$ eV). Thus, it is the S-enrichment and its partial oxidation on the CdS gel surface that leads synergistically to enhanced NO_2 adsorption, addressing Factor 2. For the third factor, NO_2 adsorption events are transduced to an electrical signal by altering the charge carrier concentration in the space charge layer of the CdS gel. According to the DFT results in **Figure 5g**, the degree of charge transfer between a CdS surface and an adsorbed NO_2 is positively correlated with $\Delta E_{ads}(NO_2)$, suggesting the unique surface features of the CdS gel also benefit the signal transduction. A closer look at the differential electron density of NO_2 adsorption on the CdS gel surface reveals that oxidized S sites are engaged in promoting the electron transfer from CdS to the adsorbed NO_2 (**Figure 5h** and **Figure S12**). The depletion of electrons creates more holes in the valance band of CdS and substantially promotes its conductivity due to the p-type semiconducting nature of the CdS gel (**Figure 5a**-**c**). Additionally, the small crystallite size of CdS QDs within the gel network also facilitates signal transduction because the gas sensitivity increases steeply as the crystallite size decreases to $\leq 2L$, where L is the depth of the space-charge layer, ~60 nm for CdS, far larger than the QDs that make up the gel.[51, 52]

DFT calculations were also used to shed light on the origin of the selectivity of CdS gels towards NO_2. **Figure 5i** shows the calculated adsorption energies (ΔE_{ads}) of the nine gases or vapors tested in our experiments on a CdS surface (purple hashes on the left), as well as the calculated charge transferred between the CdS surface and adsorbed gas (bars on the right, orange = charge transfer from CdS; green = charge transfer to CdS). While the trends in absorption energies do not correlate with activity, we recognized similar patterns between the charge transfer values in **Figure 5i** and the sensor responses in **Figure 5f**, which suggests the high selectivity towards NO_2 originates from the significant charge transfer from CdS to NO_2. We also found that adsorption and charge transfer to NO_2 was enhanced by the presence of a Cd vacancy (S-rich surface) and S oxidation, relative to other analytes (potentially interfering gases), which also contributes to the superior selectivity of the CdS gel towards NO_2 sensing (**Figures S13** to **S15**).

SUMMARY AND CONCLUSIONS

For the first time, we demonstrate a general and facile electrochemical method to crosslink metal chalcogenide QDs into a gel. Electrochemically prepared QD monolithic gels are mesoporous with a large surface area of 220 m^2/g and an average pore diameter of 20 nm. The gel network retains the crystalline structures of its QD building blocks, and the monolith remains quantum-confined. Mechanistic studies using electrochemistry and spectroscopy have revealed a three-step electrogelation mechanism: first, electrochemical removal of thiolate ligands; second, spontaneous metal ion dissolution; and third, electrochemical crosslinking of QDs by dichalcogenide bond formation. For thioglycolate-capped CdS QDs, the thiolate ligand removal occurs at ~0.8 V, and the subsequent crosslinking takes place at a higher potential of 1.2 V. The highly open and interconnected structure of the semiconducting QD gel provides a large area of target–receptor interfaces and facile charge transport, which makes them ideal candidates for applications in gas-sensing and catalysis. As proof of principle, we show a one-step preparation of CdS gel sensors and their use for NO_2 gas sensing at room temperature. The CdS gel exhibits exceptional NO_2 sensing performance with an ultralow limit of detection of 11 ppb, a short response and recovery time of < 30 s, a small variation in response of ~7% during 400 NO_2 exposure/removal cycles, a remarkable device-to-device variation of < 5%, and a superior selectivity towards NO_2. DFT calculations show that the unique surface features of the CdS gel significantly contribute to its outstanding sensing performance. The ability to adjust compositional and surface characteristics of electrogels through parameterization suggests these materials can be a flexible platform for a range of applications exploiting the combination of interconnected matter-pore network and robust charge transport.

Supporting information

The Supporting Information is available free of charge on the ACS Publications website.

Experimental methods for CdS, ZnS, and CdSe QD syntheses, chemical gelation, electrogelation, preparation of aerogels, gel sensor fabrication, characterization and measurements, gas sensing tests, and computational calculations; CdS QD size distribution; a photograph of electrogelation of 11-mercapto-undecanoate-capped CdS QDs; photographs of electrogelation of CdS QDs under various conditions; finite element simulation of the *iR* drop in a gel; TEM images of the CdS+C sample; XPS peak fitting results of CdS QDs, chemgel, and electrogel; fabrication and characterization of a CdS gel sensor; photograph of the home-built gas sensing test apparatus; a typical response-recovery curve for a gel sensor; XPS spectra of a gel sensor; DFT calculated differential valence-electron charge densities, adsorption energy, charge transfer, and optimized adsorption binding geometries; BET analysis data for chemgel and electrogel; comparison between the CdS gel sensor and 100 state-of-the-art room-temperature NO_2 gas sensors in literature; the device-to-device variations of CdS gel sensors.

AUTHOR INFORMATION

Corresponding Author

*zhangbright@tsinghua.edu.cn
*sbrock@chem.wayne.edu
*long.luo@wayne.edu

Author Contributions

‡These authors contributed equally: Chathuranga C. Hewa-Rahinduwage, Xin Geng, Karunamuni L. Silva.

The authors declare no competing financial interest.

ACKNOWLEDGMENTS

This work was financially supported by the start-up funds of L. Luo from Wayne State University and a National Science Foundation (NSF) grant of S. L. Brock (Grant number CHE-1709776). The authors thank E. Nikolla at Wayne State University for performing the Surface Area Analysis measurements, T. Ma at Michigan Center for Materials Characterization, University of Michigan, for TEM imaging using a JEOL3100R05 funded by NSF grant #DMR-0723032, and X. Yu at Wayne State University for the AFM imaging. This work also made use of an XPS that is partially funded by NSF grant #1849578, a JEOL-2010 TEM supported by NSF grant #0216084, and the PXRD Facility supported by NSF grant #1427926.

REFERENCES

1. J. Owen and L. Brus, *J. Am. Chem. Soc.*, 2017, **139**, 10939-10943.
2. C. Pu, H. Qin, Y. Gao, J. Zhou, P. Wang and X. Peng, *J. Am. Chem. Soc.*, 2017, **139**, 3302-3311.
3. G. H. Carey, A. L. Abdelhady, Z. Ning, S. M. Thon, O. M. Bakr and E. H. Sargent, *Chem. Rev.*, 2015, **115**, 12732-12763.
4. E. H. Sargent, *Nat. Photonics*, 2012, **6**, 133-135.
5. N. Razgoniaeva, P. Moroz, S. Lambright and M. Zamkov, *J. Phys. Chem. Lett.*, 2015, **6**, 4352-4359.
6. J. M. Pietryga, Y.-S. Park, J. Lim, A. F. Fidler, W. K. Bae, S. Brovelli and V. I. Klimov, *Chem. Rev.*, 2016, **116**, 10513-10622.
7. C. R. Kagan, E. Lifshitz, E. H. Sargent and D. V. Talapin, *Science*, 2016, **353**, aac5523.
8. D. Wen and A. Eychmüller, *Chem. Commun.*, 2017, **53**, 12608-12621.
9. M. A. Boles, M. Engel and D. V. Talapin, *Chem. Rev.*, 2016, **116**, 11220-11289.
10. J. J. Urban, D. V. Talapin, E. V. Shevchenko and C. B. Murray, *J. Am. Chem. Soc.*, 2006, **128**, 3248-3255.
11. S.-H. Jung, C. Chen, S.-H. Cha, B. Yeom, J. H. Bahng, S. Srivastava, J. Zhu, M. Yang, S. Liu and N. A. Kotov, *J. Am. Chem. Soc.*, 2011, **133**, 10688-10691.
12. Z. Tang, N. A. Kotov and M. Giersig, *Science*, 2002, **297**, 237.
13. S. Ghosh and L. Manna, *Chem. Rev.*, 2018, **118**, 7804-7864.
14. M. V. Kovalenko, M. Scheele and D. V. Talapin, *Science*, 2009, **324**, 1417.
15. J. Chang and E. R. Waclawik, *RSC Advances*, 2014, **4**, 23505-23527.
16. J.-Y. Kim and N. A. Kotov, *Chem. Mater.*, 2014, **26**, 134-152.
17. I. U. Arachchige and S. L. Brock, *Acc. Chem. Res*, 2007, **40**, 801-809.
18. I. R. Pala, I. U. Arachchige, D. G. Georgiev and S. L. Brock, *Angew. Chem., Int. Ed.*, 2010, **49**, 3661-3665.
19. J. L. Mohanan, I. U. Arachchige and S. L. Brock, *Science*, 2005, **307**, 397.
20. H. Yu, R. Bellair, R. M. Kannan and S. L. Brock, *J. Am. Chem. Soc.*, 2008, **130**, 5054-5055.
21. I. U. Arachchige and S. L. Brock, *J. Am. Chem. Soc.*, 2007, **129**, 1840-1841.
22. J. L. Davis, A. M. Chalifoux and S. L. Brock, *Langmuir*, 2017, **33**, 9434-9443.
23. L. D. Gelb and K. Gubbins, *Langmuir*, 1998, **14**, 2097-2111.
24. E. P. Barrett, L. G. Joyner and P. P. Halenda, *J. Am. Chem. Soc.*, 1951, **73**, 373-380.
25. K. Rajeshwar, N. R. de Tacconi and C. R. Chenthamarakshan, *Chem. Mater.*, 2001, **13**, 2765-2782.
26. Q. Yao, I. U. Arachchige and S. L. Brock, *J. Am. Chem. Soc.*, 2009, **131**, 2800-2801.
27. A. J. Bard and L. R. Faulkner, *Electrochemical methods: fundamentals and applications*, Wiley New York, 1980.
28. L. Korala and S. L. Brock, *J. Phys. Chem C*, 2012, **116**, 17110-17117.
29. G. Kister, G. Cassanas and M. Vert, *Spectrochim. Acta A*, 1997, **53**, 1399-1403.
30. K.-i. Ataka and M. Osawa, *Langmuir*, 1998, **14**, 951-959.
31. A. Veamatahau, B. Jiang, T. Seifert, S. Makuta, K. Latham, M. Kanehara, T. Teranishi and Y. Tachibana, *Phys. Chem. Chem. Phys.*, 2015, **17**, 2850-2858.
32. M. Lichtensteiger, C. Webb and J. Lagowski, *Surf. Sci.*, 1980, **97**, L375-L379.
33. I. U. Arachchige and S. L. Brock, *J. Am. Chem. Soc.*, 2006, **128**, 7964-7971.
34. L. Korala, L. Li and S. L. Brock, *Chem. Commun.*, 2012, **48**, 8523-8525.
35. L. Korala, Z. Wang, Y. Liu, S. Maldonado and S. L. Brock, *ACS Nano*, 2013, **7**, 1215-1223.
36. Q. Yao and S. L. Brock, *Nanotechnology*, 2010, **21**, 115502.
37. W. Jiao, G. Hagler, R. Williams, R. Sharpe, R. Brown, D. Garver, R. Judge, M. Caudill, J. Rickard, M. Davis, L. Weinstock, S. Zimmer-Dauphinee and K. Buckley, *Atmos. Meas. Tech.*, 2016, **9**, 5281-5292.
38. H.-J. Kim and J.-H. Lee, *Sens. Actuators B: Chem.*, 2014, **192**, 607-627.
39. L. Huang, Z. Wang, J. Zhang, J. Pu, Y. Lin, S. Xu, L. Shen, Q. Chen and W. Shi, *ACS Appl. Mater. Interfaces*, 2014, **6**, 7426-7433.
40. M. Bao, Y. Chen, F. Li, J. Ma, T. Lv, Y. Tang, L. Chen, Z. Xu and T. Wang, *Nanoscale*, 2014, **6**, 4063-4066.
41. C. Jiang, G. Zhang, Y. Wu, L. Li and K. Shi, *CrystEngComm*, 2012, **14**, 2739-2747.
42. M. C. McAlpine, H. Ahmad, D. Wang and J. R. Heath, *Nat. Mater.*, 2007, **6**, 379-384.
43. B. Liu, L. Chen, G. Liu, A. N. Abbas, M. Fathi and C. Zhou, *ACS Nano*, 2014, **8**, 5304-5314.
44. T. Pham, G. Li, E. Bekyarova, M. E. Itkis and A. Mulchandani, *ACS Nano*, 2019, **13**, 3196-3205.
45. J. Liu, S. Li, B. Zhang, Y. Wang, Y. Gao, X. Liang, Y. Wang and G. Lu, *J. Colloid Interface Sci.*, 2017, **504**, 206-213.
46. W. Li, X. Geng, Y. Guo, J. Rong, Y. Gong, L. Wu, X. Zhang, P. Li, J. Xu and G. Cheng, *ACS Nano*, 2011, **5**, 6955-6961.
47. P. Qi, O. Vermesh, M. Grecu, A. Javey, Q. Wang, H. Dai, S. Peng and K. Cho, *Nano Lett.*, 2003, **3**, 347-351.
48. S. Cui, H. Pu, S. A. Wells, Z. Wen, S. Mao, J. Chang, M. C. Hersam and J. Chen, *Nat. Commun.*, 2015, **6**, 8632.
49. N. Yamazoe, *Sens. Actuators B: Chem.*, 2005, **108**, 2-14.
50. N. Leventis, I. A. Elder, D. R. Rolison, M. L. Anderson and C. I. Merzbacher, *Chem. Mater.*, 1999, **11**, 2837-2845.
51. C. Xu, J. Tamaki, N. Miura and N. Yamazoe, *Sens. Actuators B: Chem.*, 1991, **3**, 147-155.
52. X. K. Zhao, L. McCormick and J. H. Fendler, *Chem. Mater.*, 1991, **3**, 922-935.

TOC